



UvA-DARE (Digital Academic Repository)

Carotid single- and dual-layer stents reduce the wall adhesion of platelets by influencing flow and cellular transport

Spieker, C.J.; Kern, A.Y.; Korin, N.; Mangin, P.H.; Hoekstra, A.G.; Závodszky, G.

DOI

[10.1016/j.combiomed.2024.109313](https://doi.org/10.1016/j.combiomed.2024.109313)

Publication date

2024

Document Version

Final published version

Published in

Computers in Biology and Medicine

License

CC BY-NC

[Link to publication](#)

Citation for published version (APA):

Spieker, C. J., Kern, A. Y., Korin, N., Mangin, P. H., Hoekstra, A. G., & Závodszky, G. (2024). Carotid single- and dual-layer stents reduce the wall adhesion of platelets by influencing flow and cellular transport. *Computers in Biology and Medicine*, 183, Article 109313. <https://doi.org/10.1016/j.combiomed.2024.109313>

General rights

It is not permitted to download or to forward/distribute the text or part of it without the consent of the author(s) and/or copyright holder(s), other than for strictly personal, individual use, unless the work is under an open content license (like Creative Commons).

Disclaimer/Complaints regulations

If you believe that digital publication of certain material infringes any of your rights or (privacy) interests, please let the Library know, stating your reasons. In case of a legitimate complaint, the Library will make the material inaccessible and/or remove it from the website. Please Ask the Library: <https://uba.uva.nl/en/contact>, or a letter to: Library of the University of Amsterdam, Secretariat, P.O. Box 19185, 1000 GD Amsterdam, The Netherlands. You will be contacted as soon as possible.

UvA-DARE is a service provided by the library of the University of Amsterdam (<https://dare.uva.nl>)



Carotid single- and dual-layer stents reduce the wall adhesion of platelets by influencing flow and cellular transport

Christian J. Spieker^{a,1}, Axelle Y. Kern^{b,1}, Netanel Korin^c, Pierre H. Mangin^b, Alfons G. Hoekstra^a, Gábor Závodszy^{a,*}

^a Computational Science Lab, Informatics Institute, Faculty of Science, University of Amsterdam, Amsterdam, The Netherlands

^b INSERM, EFS Grand-Est, BPPS UMR-S 1255, FMTS, Université de Strasbourg, Strasbourg, France

^c Department of Biomedical Engineering, Technion—Israel Institute of Technology, Haifa, Israel

ARTICLE INFO

Keywords:

Carotid artery stenting
Single-layer stent
Dual-layer stent
Stent thrombosis
Cellular blood

ABSTRACT

An ongoing thrombosis on a ruptured atherosclerotic plaque in the carotid may cause stroke. The primary treatment for patients with tandem lesion is stenting. Dual-layer stents have been introduced as an alternative to single-layer stents for elective and emergent carotid artery stenting. While the dual-layer structure shows promise in reducing plaque prolapse through the stent struts and with it the occurrence of post-procedural embolism, there are early signs that this newer generation of stents is more thrombogenic. We investigate a single- and a dual-layer stent design to assess their influence on a set of thrombosis-related flow factors in a novel setup of combined experiments and simulations. The *in vitro* results reveal that both stents reduce thrombus formation by approximately 50% when human anticoagulated whole blood was perfused through macrofluidic flow chambers coated with either collagen or human atherosclerotic plaque homogenates. Simulations predict that the primary cause is reduced platelet presence in the vicinity of the wall, due to the influence of stents on flow and cellular transport. Both stents significantly alter the near-wall flow conditions, modifying shear rate, shear gradient, cell-free zones, and platelet availability. Additionally, the dual-layer stent has further increased local shear rates on the inner struts. It also displays increased stagnation zones and reduced recirculation between the outer-layer struts. Finally, the dual-layer stent shows further reduced adhesion over an atherosclerotic plaque coating. The novel approach presented here can be used to improve the design optimization process of cardiovascular stents in the future by allowing an in-depth study of the emerging flow characteristics and agonist transport.

1. Introduction

Vascular stents are commonly deployed in an angioplastic procedure to treat the occlusion or stenosis of arteries, such as the coronary, femoral or carotid artery. In this procedure, the stent is expanded at the site of obstruction to restore the vascular lumen and re-establish unrestricted blood flow to avoid otherwise potentially fatal side effects of vascular stenosis such as heart attack or stroke [1–5]. An ongoing thrombosis in the carotid artery has a high likelihood of leading to a stroke, due to the proximity to the brain. The pathologic flow conditions of the stenosed segment favour thrombosis and ultimately embolism. The main treatment options for carotid stenosis are carotid endarterectomy and carotid artery stenting (CAS) [6]. Elective CAS is performed on patients with carotid stenosis to decrease the possibility for stroke in the future and emergent CAS can be applied as a treatment

during acute ischemic stroke [7]. Additionally, CAS can be deployed in combination with cerebral protection devices to act as a filter reducing the incidence of microemboli that disseminate during the procedure and increase the risk for neurological complications, such as periprocedural stroke [8,9]. However, the utilization of vascular stents introduces additional risks, stent thrombosis (ST) being among the most common complications.

Acute early carotid ST, occurring within 24 h post-stenting, is a potentially fatal complication with a recorded incidence of 0.5–0.8% in elective CAS [10]. ST following emergent CAS during stroke thrombectomy demonstrates significantly higher occurrences, with a recorded incidence between 8 to 28%, depending on the accompanying treatment [11–13]. Advancements in antithrombotic therapy, most notably dual-antiplatelet therapy, have decreased the risk for early ST, occurring within 30 days post-stenting. At the same time

* Corresponding author.

E-mail address: G.Zavodszy@uva.nl (G. Závodszy).

¹ C.J.S. and A.Y.K. contributed equally to this work.

such therapies can have an adverse effect by increasing the likelihood for bleeding complications, especially for stroke patients, in whom hemorrhagic stroke transformation may occur [14]. In addition to this, improvements in stent deployment techniques, such as post-dilation, have further decreased early ST risk. Nevertheless, ST, in particular late and very late ST (between 30 days - 1 year and after 1 year post-stenting, respectively), remains a common fatal cause of post-stenting complications, where the rapid closure of the vessel leads to stroke, acute myocardial infarction or sudden cardiac death depending on the location of the vessel [15–18].

Major factors that influence the risk for ST are patient specific characteristics, the material of the stent (DES, bare metal stent (BMS) or bioresorbable vascular scaffolds (BVS)) and the accompanying therapy. Additional factors that affect the ST risk are a possible misalignment of the stent, in the form of stent malapposition or scaffold dismantling for BVS, and the design of the stent [19–21]. Stent designs differ widely in form, composition and geometrical structure. Common structures include single- or multi-layered metal alloy wires that are braided, knitted or welded into a cylindrical shape. In addition to single-layered carotid stents, a new generation of dual-layered stents have been introduced, with the anticipated benefit of reducing plaque prolapse through the stent struts and post-procedural embolism by adding an inner layer strut mesh with smaller free cell areas [22,23]. While this seems to be effective in preventing plaque prolapse [24,25], a small-scale study by Yilmaz et al. indicates that stents with a dual-layer design have a higher occurrence of acute vessel occlusion in comparison to stents with a single-layer structure when applied in emergent CAS [26]. Additionally, recent work by Sykora et al. is reporting the restenosis rate for patients treated with dual-layer carotid stents to be significantly higher in comparison to single-layer stents [27]. Overall, the introduction of dual-layer stents in CAS is recent and their ST risk compared to single-layer stents is unclear.

ST thrombi are a heterogeneous composition of platelets, fibrin, red blood cells (RBCs) and white blood cells [28]. Though the composition can differ depending on the stented vessel, the type of stent used and patient-specific immune response, the largest fraction of the thrombi is made up of platelets and fibrin [28–30]. Initial clot formation thrombosis is set off by the rapid aggregation of platelets in high shear environments and the reinforcement of the clot through fibrin formation. This initial aggregation is commonly mediated via entanglement with von Willebrand factor (VWF) molecules and fibrinogen which are present in ST thrombi as well [28,31,32].

Computational simulations have found a broad utilization in studying stent design [33,34] and deployment [35] as well as related pathologies, such as in-stent restenosis [36–38] and ST [39,40]. Jiménez et al. presented a purely continuous flow-based stent strut design study, discussing the effects of strut embedment depth and shape on recirculation regions proximal and distal to the strut in regards to flow direction [34]. In a more recent work, Chesnutt et al. are considering cellular flow to investigate the initiation of ST in coronary artery stenting. The mesoscale model utilizes the discrete element method to simulate platelet interactions, including their activation state, around misaligned struts [39,40].

The current work investigates two clinically used carotid stents – a single-layer and a dual-layer one – to assess the effect of their design differences on cellular flow behaviour that is potentially related to ST by evaluating a complementing *in vitro* and *in silico* setup. The former introduces a novel macrofluidic carotid artery flow chamber [41] to perform aggregation intensity measurements on adhesive surface coatings. The complementing simulations are setup in a multiscale framework to enable capturing the size of the whole stent, while also allowing to infer cellular behaviour around the stent struts. Macroscale continuum flow simulations of entire stented carotid vessel segments are performed to compute the bulk flow behaviour. Information from the bulk flow is then used as a boundary condition for the microscale cellular simulations around the strut segments of the two carotid stent

designs. To the best of the authors' knowledge, no cellular-level study has yet explored the differences between single-layer and dual-layer carotid stent designs.

The simulations of both stented segments display a reduced platelet availability in vicinity to the vessel wall when compared to a non-stented reference setup. The same trend is reflected in the *in vitro* experiments. When comparing the single- to the dual-layer design, the simulations further show, that the introduction of an inner strut layer in the dual-layer design elevates local shear rate and rate of elongation magnitude on top of the inner layer struts, while also decreasing the wall shear rate. Additionally, a change in local platelet distribution can be observed in the vicinity of the wall, in conjunction with larger stagnation zones and reduced recirculation regions around the outer layer struts of the dual-layer design. The cell resolved simulations reveal the significant influence that the recirculation regions around the stent struts have on local cell distributions. These factors might play an important role in the future development of stent designs aiming to reduce ST: optimizing the shape of the recirculation regions by small adjustments to the strut arrangement could significantly influence the local platelet availability and with it the risk for ST.

2. Materials and methods

The effects of carotid stent design on cellular flow behaviour are assessed via *in vitro* platelet surface coverage experiments and by evaluating differences in local flow profiles and cell distributions observed through blood flow simulations. The experiments are performed in a novel carotid artery chamber, where the stented segment is coated with either a human carotid atherosclerotic plaque homogenate (HAP) or collagen. The simulations are setup in a multiscale framework, where continuum fluid simulations of the entire stented geometry are performed to capture properties of the bulk flow in the whole extent of the stent. Bulk flow behaviour information is used to extract boundary conditions for microscale cell-resolved simulations, which are deployed around the strut segments of the two carotid stent designs.

In the experimental work, two commercially available carotid stent designs, namely Carotid Wallstent (Boston Scientific, Natick, Massachusetts, USA) and Casper RX (MicroVention/ Terumo, Aliso Viejo, California, USA), are compared to each other, as well as to a *reference* case without a stent. Wallstent is a single-layer mesh stent, consisting of overlaying cobalt – chromium alloy struts, creating around 1.09 mm² large rhomboid-shaped free cell areas when the stent is open. Casper is a dual-layer nickel – titanium alloy mesh with approximately 6.1 mm² large outer layer free cell areas containing 16 × 0.38 mm² large inner free cell areas each, in the open state. Both stent types are deployed in carotid stenting procedures.

In the interest of conciseness the stent designs are subsequently referred to as *single-layer* and *dual-layer* stent design for both experiments and simulations.

2.1. *In vitro* experimental setup

The macrofluidic perfusion system is a closed circular model consisting of a peristaltic pump (Watson-Marlow, La-Queue-Les-Yvelines, France), a water bath and an elastomer chamber placed under a fluorescence microscope linked to a computer (see Fig. 1) [41]. The silicone elastomer chamber reproduces the average dimensions of the human carotid artery, with a diameter of 6 mm for the common carotid artery [42]. The carotid chambers are coated with either Horm-type collagen (200 µg/mL) or HAP (16.5 mg/mL of proteins wet weight) and either stent type, *single-layer* Wallstent or *dual-layer* Casper, is inserted subsequently. Additional experiments are performed without inserting the stent, to function as a *reference* case. Perfusion is performed at a flow rate of 380 mL/min, the human reference of carotid blood flow [43]. During blood perfusion, images are taken every 15 s automatically with Las X (Leica) to quantify platelet aggregation over time. Images are also taken after cleaning the chamber with PBS and quantify platelet aggregation at the end-point.

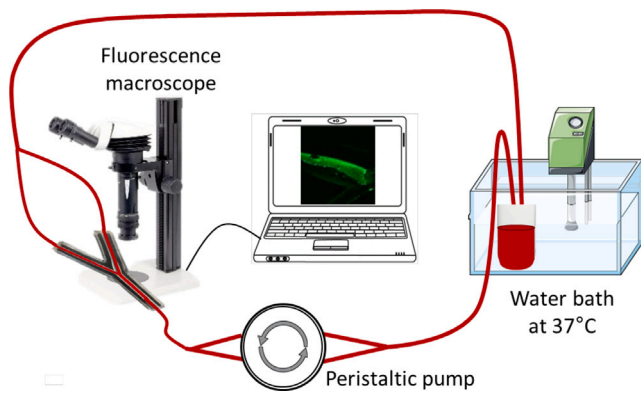


Fig. 1. Schematic of the *in vitro* experimental setup, including circulation of blood through the carotid chamber, a water bath and a peristaltic pump. The elastomer carotid chamber is placed under a fluorescence microscope linked to a computer to capture images of the platelet surface coverage.

Blood donation

The study is conform to the ethical standards of the Declaration of Helsinki. All blood donors gave their free and informed written consent to participate and were healthy volunteers. Blood (45 mL) is collected in a tube containing hirudin (5 mL, final concentration: 100 U/mL) (Transgene, Illkirch-Graffenstaden, France) and kept at 37 °C. The first couple mL of blood are discarded. Legal and ethical authorization for the use of collected blood for research was obtained through a national convention between the French National Institute of Health and Medical Research (INSERM) and the French Blood Institute (EFS) (convention number I/DAJ/C2675).

Macrofluidic flow chamber mimicking the carotid artery

The dimensions of the carotid flow chamber are based on the well-known average dimensions of the lumen of human carotid (common, internal and external carotids). The fabrication of the chamber has been described previously [41].

Flow experiments in the macrofluidic flow chamber

The chamber is passivated with 3 mL of 1% HSA (Sigma-Aldrich, Lyon, France) for 30 min at room temperature. Chambers are rinsed with PBS supplemented with CaCl₂ (2 mmol/L) and MgCl₂ (1 mmol/L) (ThermoFisher Scientific Illkirch-Graffenstaden, France; Sigma-Aldrich, Lyon, France). A Casper stent or a Wallstent is placed into the chamber using a catheter as in clinics. The flow system is composed of tubing, connectors, the peristaltic pump, the chamber and a water bath as described previously by Kern et al. [41]. The system is primed with 1X PBS at a flow rate of 380 mL/min (mean average flow rate in human carotid [43] to remove air bubbles and check for the absence of leaks. Human whole blood collected on hirudin (100 U/mL) and incubated with DiOC₆ (1 μmol/L) (Molecular Probes, Paisley, United Kingdom) to label platelets, is then perfused for 10 min through the flow chamber. Real-time visualization of platelet adhesion and thrombus formation is performed with a fluorescence microscope (Leica Microsystems, Nanterre, France).

Quantification of platelet aggregates

The images were analysed to quantify the fluorescent surface that corresponds to the platelet aggregates. The edges of the flow chamber are identified manually on the images and a measurement is made to obtain the whole area. A threshold is then set to cover the platelet aggregates formed to determine the surface attachment area of the aggregates. The ratio of the fluorescent area to the total area is used to quantify and compare the platelet aggregation under different conditions.

Human atherosclerotic plaque homogenate preparation

Carotid human atherosclerotic plaques are recovered from the department of vascular surgery of the Hospital of Strasbourg. Plaques are cryo-grinded with liquid nitrogen and a mortar to obtain a fine powder. Powder is put in a 15 mL Falcon tube and PBS (ThermoFisher Scientific, Illkirch-Graffenstaden, France) is added at a rate of 4 mL per gram of powder. The mixture is homogenized by gently stirring the tube and then undergoes 20 cycles of sonication (Bioruptor Vibra cell 75115, Sonics & Materials, Newtown, CT, USA) at an amplitude of 30%, each cycle lasting 15 s alternating with 10 s of rest to avoid overheating the system. Homogenization of the mixture is carried out at intervals of 5 cycles. As this process can generate heat, the 15 mL Falcon tube is placed in a 50 mL Falcon tube filled with ice and water. The resulting homogenate is centrifuged at 2240 G for 10 min at a temperature of 4 °C. The layer of interest is removed, weighed and resuspended at 16.5 mg protein/mL wet weight in PBS [44]. Five different plaques are mixed to obtain an homogenate to use for coating.

Statistics

Results are expressed as the mean ± standard error of the mean. Statistical analyses are performed using GraphPad Prism software (La Jolla, CA, USA). Statistical significance between different groups was assessed by the one-way ANOVA test or the Kruskal-Wallis test, according if they follow a Gaussian law or not, respectively. The $p < 0.05$ values are considered significant (* $p < 0.05$, ** $p < 0.01$, *** $p < 0.001$).

2.2. Multiscale simulation setup

The simulations are setup in a one-way coupled multiscale framework. Macroscale continuum fluid simulations are setup to supply bulk flow information as a velocity boundary condition to microscale cell-resolved simulations. The geometrical constraints are informed by literature and the experimental setup [45,46]. The multiscale setup is visualized in Fig. 2.

Continuum fluid simulation setup

Initially, macroscale simulations of a stented carotid artery segment are performed using the finite element method-based commercial computational fluid dynamics (CFD) software COMSOL Multiphysics 6.1 (COMSOL AB). To prepare the geometry for COMSOL, the open stents are rebuild in the computer-aided design (CAD) software Autodesk Fusion 360 (version 2.0.17457, Autodesk Inc.) based on dimensions from the manufacturers and literature. The open *single-layer* and *dual-layer* stents have a diameter of 8 mm each and a length of 29 and 30 mm, respectively. The large struts of the *single-layer* stent are 195 μm in diameter opposed to 180 μm for the *dual-layer* design. Since the focus is on the difference between *single-* and *dual-layer* designs, the larger struts are set to the same diameter of 180 μm. This reduces the original strut diameter of the *single-layer* design by 7.7%, which is expected to have a negligible effect. The smaller inner layer stent struts of the *dual-layer* design have a diameter of 42 μm. The radial strut distance and helix pitch of the individual struts are set to match the respective strut free cell areas and the angles between overlapping struts of the fully open stents [45,46]. Consequently, the open *single-layer* stent CAD geometry consists of 20 individual struts - 10 left-handed and 10 right-handed - arranged at a 36° radial strut distance with a 9.67 mm large helix pitch. The *dual-layer* stent contains 6 large outer layer and 18 inner layer struts in each rotation direction with a 15 mm large helix pitch each and arranged at 60 and 15° radial strut distance, respectively. Finally, the CAD geometry of the *dual-layer* design is modified to avoid highly skewed mesh elements at the tangential edge interface of the two strut layers [47,48]. To achieve this, every fourth inner layer strut of the *dual-layer* stent geometry, set to match the 60° radial interval of the outer layer struts, is omitted. For the same reason, all remaining inner layer struts are embedded into the outer layer struts by 1/4 of

Table 1

Stent and stented vessel dimensions for experiments and macroscale simulations. Experimental dimensions of the *single-layer* and *dual-layer* stent design refer to Wallstent and Casper stent dimensions, respectively. The experimental parameters: stent diameter, stent length, free cell area and strut angle refer to the open state of the stents. Multiple values for *dual-layer* stent dimensions refer to the outer and inner layer struts of the stent, respectively.

Stent design	Experimental dimensions						Simulation dimensions			
	Stent diameter (mm)	Stent length (mm)	Strut diameter (μm)	Free cell area (mm^2)	Angle ($^\circ$)	Vessel diameter (mm)	Implanted length (mm)	Stent diameter (mm)	Radial strut distance ($^\circ$)	Helix pitch (μm)
Single-layer	8	29	195	1.09	130-140	6	48	6	36	16
Dual-layer	8	30	180, 42	6.1, 0.38	105-115	6	45	6	60, 15	22.5

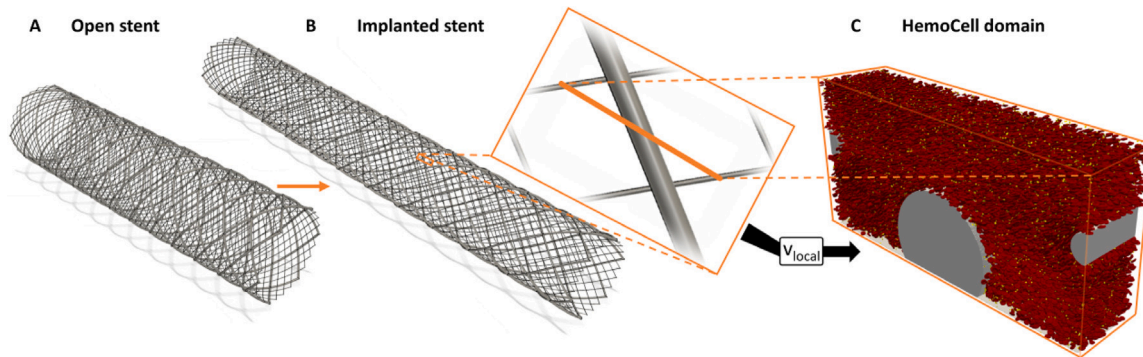


Fig. 2. One-way coupled multiscale simulation setup visualized by using the *dual-layer* stent case as an example. (A): fully open stent geometry at 8 mm diameter. (B): Implanted stent geometry at 6 mm diameter with inset to visualize the selected region for the idealized microscale simulations. (C): Visualization of microscale simulation in HemoCell at final time step $t = 1$ s, driven by velocity boundary condition extracted from continuum fluid COMSOL simulation.

the inner strut diameter. Furthermore, the braided nature of the struts is neglected in the CAD models of both stent designs and instead struts within the same layer are fully intersecting.

In alignment with the *in vitro* experiments, the simulated carotid artery segment is set to a diameter of 6 mm. Since the diameter is smaller than the open stent diameter, the stent is restricted from full expansion during deployment. To compensate for this partial compression, the stent remains elongated compared to the fully open state, which changes the stent strut alignment and subsequently the shape and area of the stent strut free cells. To account for this change in the simulation, the CAD models are adjusted for implanted stent dimensions by decreasing the stent diameter and increasing the stent length accordingly, while maintaining the radial strut distance and adjusting the helix pitch to preserve the revolution count of the struts (see Fig. 2A and B). The main experimental and simulation dimensions are summarized in Table 1.

The compression of the stent is exerted as a radial force of the stent struts on the vessel wall, which causes the elastic carotid artery wall to stretch and be displaced at the location of stent struts [49]. This resulting embedment of the stent into the vessel wall is also present in RT601 silicon elastomer channels, as used in the *in vitro* experiments, albeit to a lesser degree. To account for the embedment effect in the simulations, the diameter of the compressed strut helices is chosen to be half a strut diameter larger than the vessel diameter, leading to a strut embedment of 1/4 strut diameter into the vessel wall.

The vessel surrounding the stent is simplified as a straight cylinder geometry. In addition to the *single-* and *dual-layer* stent model, a *reference* geometry without a stent, consisting of only the vessel cylinder, is set up. To account for the non-Newtonian fluid property of whole blood, the Carreau model is utilized. The model parameters for whole blood are adopted from Tabakova et al. [50]. In accordance with experimental values for whole blood, the fluid density is set to 1060 kg/m^3 [51] and the flow rate is set to 380 mL/min, matching the flow rate of the *in vitro* experiments.

For each setup - non-stented *reference*, *single-layer* and *dual-layer* stent - a stationary result is computed in COMSOL. Pulsatility is not considered in these simulations, since they are only used to retrieve

an average velocity value. Following the completed simulations, the average radial 1D velocity profiles are calculated to extract the average velocity 250 μm from the vessel wall, at radius 2.75 mm. The resulting velocity value is supplied to the microscale cellular simulations as a velocity boundary condition.

Cell-resolved simulation setup

To perform microscale blood flow simulations in the vicinity of the stent struts at the vessel wall, the open-source cell-resolved HemoCell code is used [52]. HemoCell applies the lattice Boltzmann method (LBM) as a fluid solver for blood plasma, coupled via the immersed boundary method (IBM) to the discrete element method (DEM) description of the suspended cells. The LBM is based on a discrete-velocity distribution function, realizing iterative streaming and collision steps to recover the Navier–Stokes equations with 2nd order accuracy [53, 54]. These steps are applied on a 3D Eulerian lattice representing a discretized grid of velocity populations to simulate 3D fluid flow. The LBM fluid solver implemented in HemoCell is based on the open-source Palabos (Parallel Lattice Boltzmann Solver) library [55].

In HemoCell, the velocity space is discretized in 19 directions, leading to the so called D3Q19 velocity set. The discretized lattice Boltzmann equation:

$$f_i(x + c_i \delta t, t + \delta t) = f_i(x, t) + \Omega_i(x, t) \quad (1)$$

describes the movement of particles $f_i(x, t)$ to the neighbouring point $x + c_i \delta t$ at velocity c_i during time step $t + \delta t$. Ω_i represents the collision operator, which incorporates the effect of particle collisions occurring at every time step. HemoCell uses the Bhatnagar, Groos and Krook (BGK) collision operator [56]:

$$\Omega_i(f) = -\frac{f_i - f_i^{\text{eq}}}{\tau} \delta t. \quad (2)$$

The BGK operator handles the particle collisions by relaxing the populations towards an equilibrium state f_i^{eq} . The relaxation time τ determines the rate of relaxation. The equilibrium distribution is defined by:

$$f_i^{\text{eq}}(x, t) = w_i \rho \left(1 + \frac{u \cdot c_i}{c_s^2} + \frac{(u \cdot c_i)^2}{2c_s^4} - \frac{u \cdot u}{2c_s^2} \right). \quad (3)$$

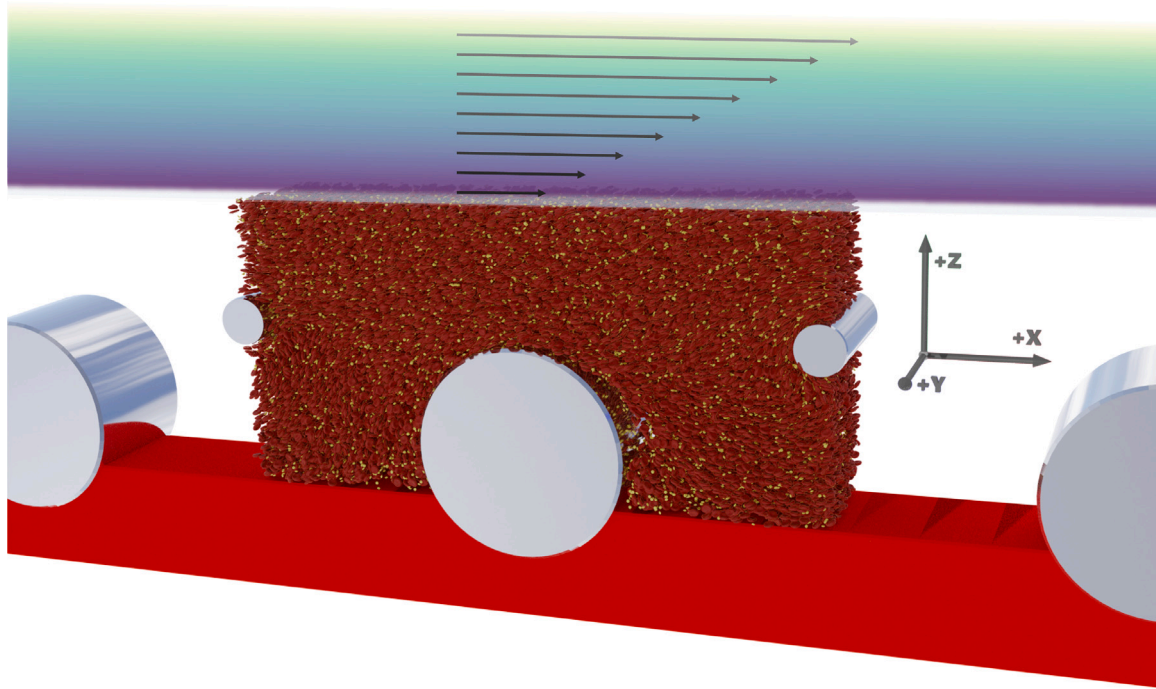


Fig. 3. Visualization of *dual-layer* case simulation in HemoCell with the strut locations in grey metallic appearance and the bottom wall coloured in red. The simulated domain is limited to the cuboid volume that contains the cells, though the periodic boundary condition in X-dimension directs the flow to continuously bypass the stent struts. The RBCs and platelets within the cuboid volume are coloured in dark red and yellow, respectively. The shear profile decreasing towards the X-Y top plane of the simulated domain represents the shear gradient from the macroscopic simulation. The velocity boundary condition of the HemoCell simulation is based on the local velocity evaluation of the COMSOL simulation.

Here, w_i represents weighting coefficients that are specific to the chosen discrete velocity set and c_s describes the lattice speed of sound. Ultimately, the equilibrium distribution f_i^{eq} only depends on the local density ρ and velocity u values. In the lattice Boltzmann algorithm of a single time step, the equations are decomposed into a collision (or relaxation) and streaming (or propagation) step.

The immersed cells in HemoCell are described by triangulated membrane meshes with a Lagrangian surface description. To couple this cellular description to the Eulerian grid of the LBM fluid, the IBM is utilized [57–59], which creates a direct connection through external force terms. The deformations of cells caused by the fluid movement are computed using a validated constitutive model and the resulting forces are applied back to the fluid. The method involves interpolation for each coupling step to transfer information between the structured fluid nodes and the unstructured cellular meshes. The deformation response of RBCs is based on a constitutive force model consisting of four force components:

$$F_{total} = F_{link} + F_{bend} + F_{area} + F_{volume}. \quad (4)$$

The F_{link} force represents the stretching and compression of the spectrin filaments making up the cytoskeleton of the interior RBC membrane. In HemoCell this spectrin cytoskeleton is represented by the edges of the surface triangles. The second force component, F_{bend} , describes the bending response of the membrane. F_{area} relates to the lipid bilayer membrane of the RBC and enforces surface conservation. The last force, F_{volume} , maintains the quasi-incompressibility of the entire RBC volume. The detailed description and validation of these force terms can be found in [60]. A simplified membrane model is employed for the smaller and more rigid platelets [60,61].

The open-source framework has been thoroughly validated in the past and has found a wide array of application, from studying fundamental cellular margination behaviour to actively modelling the platelet aggregation process [62–70].

The simulation geometry of each respective case, *reference*, *single-layer* and *dual-layer* stent, is setup to mimic a small region of the stented carotid artery segment, focused on the vicinity to the vessel wall. Each geometry consists of a $500 \times 100 \times 250 \mu\text{m}^3$ ($X \times Y \times Z$) large cuboid.

The *single-layer* case geometry includes a single strut at half the cuboid length and the *dual-layer* case geometry contains a second, inner layer, strut that is split between the in- and outlet Y-Z planes of the geometry (see Fig. 3). The strut dimensions and their embedment into the vessel wall is identical to the continuum fluid simulations (see Table 1). The flow is driven by a velocity boundary condition assigned to the X-Y top plane wall in positive X-direction, which establishes the flow profile in the local region of a stented carotid artery segment. Furthermore, periodic boundary conditions are utilized in the X- and Y-dimensions. The periodic boundary condition in X-dimension directs the flow to continuously bypass the stent struts, while the simulated geometry stays limited to only a single strut set (see Fig. 3), consequently reducing computational cost. To create planar symmetry at the in- and outlet Y-Z planes, which is necessary for the periodic boundary conditions to function correctly, the angled strut orientations are omitted and struts are instead aligned perpendicular to the flow direction. The velocity values for the velocity boundary condition are prescribed based on the continuum fluid simulations (see Fig. 2B and C).

Each case is initialized with a local hematocrit of 25% and a platelet volume concentration of 1.7% with cells placed at random positions and orientations [62]. For the *reference*, *single-layer* and *dual-layer* case this corresponds to 34,935 RBCs and 18,857 platelets, 34,673 RBCs and 18,908 platelets and 34,646 RBCs and 18,884 platelets, respectively. Individual RBCs and platelets have a volume of $90 \mu\text{m}^3$ and $11 \mu\text{m}^3$ each. The platelet concentration is significantly larger than physiological levels to increase statistical significance [71]. At 1.7% the increased platelet volume concentration is still negligible, therefore the flow dynamics remain fully governed by RBCs.

With the respective velocity boundary supplied by the macroscale continuum fluid simulations, each of the three HemoCell simulations is executed on 50 nodes (6400 cores) on the ARCHER2 UK national supercomputer (EPCC, Edinburgh, United Kingdom) for approximately 72 h of wall time to reach 1 s of simulated flow.

Subsequently, the flow profiles and cellular distributions of the simulation output are evaluated. Shear rate and rate of elongation profiles (see Spieker et al. [67–69]) are displayed as side views (X-Z plane) of the geometry. The profiles are averaged across the Y-axis

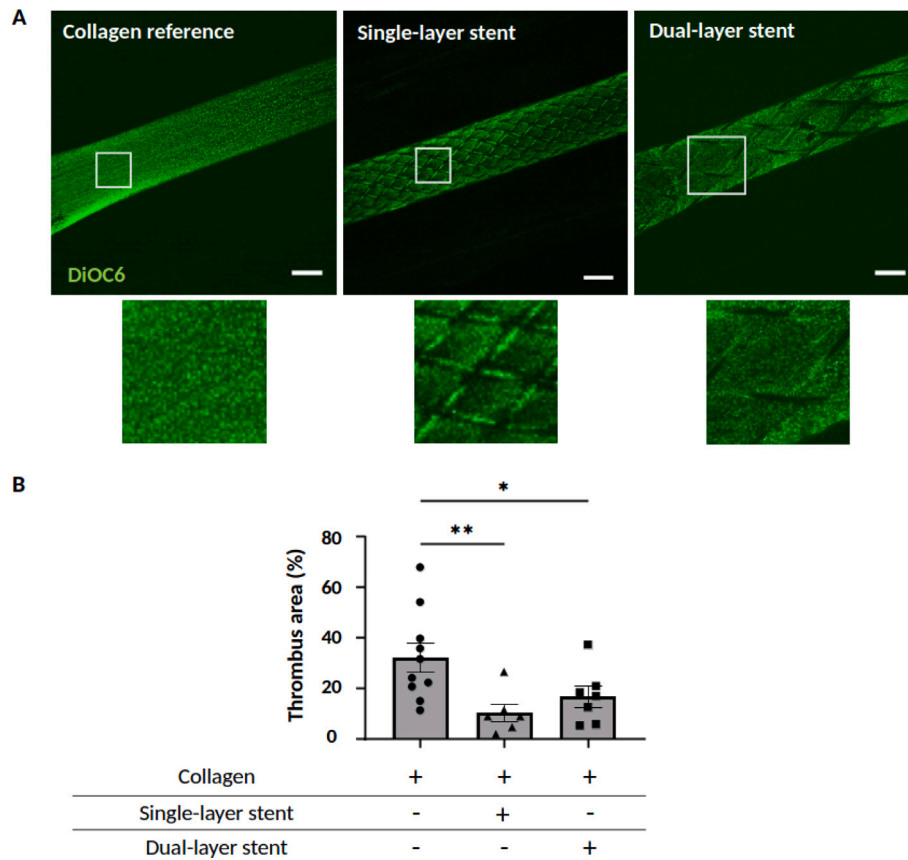


Fig. 4. Images of platelet aggregates on stents and collagen. (A) Platelet aggregation on collagen in the *reference* chamber (no stent) (left), in a chamber implanted with a *single-layer* (middle) and a *dual-layer* (right) carotid stent, after 10 min perfusion of anticoagulated whole blood labelled with DiOC₆. Scale bar: 2 mm. (B) Surface area quantification of platelet aggregation in the *reference* chamber coated only with collagen, or implanted with a *single-* or *dual-layer* stent (* $p = 0.0366$; ** $p = 0.0068$). Values are the mean \pm standard error of the mean.

and over time for iterations between 0.9–1 s. Cellular distributions are visualized from the same viewpoint, displaying average local RBC and platelet volume concentration at lattice node resolution on the X-Z plane ($0.5 \times 0.5 \mu\text{m}^2$) and across the entire Y-axis (100 μm). Additionally, platelet concentration in 4 μm vicinity to the vessel wall is quantified in a 1D distribution plot across the X-axis by reducing bins in Z-direction to a single instance ranging from 0–4 μm . In this case, cellular distributions are time averaged between 0.5–1 s.

3. Results

3.1. In vitro results

Stent implantation reduces thrombus formation on both collagen and human atherosclerotic plaque homogenates. The two braided *single-* and *dual-layer* stents are studied and compared to a non-stented *reference* case. In a chamber coated with type-I fibrillar collagen (200 $\mu\text{g}/\text{mL}$) a clear signal accumulating over time is observed, which is explained by the formation and the accumulation of platelets aggregates (see Fig. 4A). Unexpectedly, when blood is perfused through the collagen-coated chamber implanted with the *single-* or *dual-layer* stent, epifluorescence images indicate a decreased fluorescent signal for both cases (see Fig. 4A). This observation is confirmed by a quantification, indicating a reduction of 68% and 48% respectively of the size of platelet aggregates as compared to the control with no stent implantation (*reference* collagen: $32.2 \pm 5.6\%$; *single-layer* stent: $10.4 \pm 3.5\%$; *dual-layer* stent: $16.7 \pm 4.1\%$; $p = 0.0151$) (see Fig. 4B). This result suggests that a stent can exhibit an antithrombotic effect by reducing platelet accumulation in a diseased vessel.

To extend this result, similar experiments in which collagen is replaced by human atherosclerotic plaque (HAP) homogenates are performed to better mimic the presence of atherosclerotic plaque exposing a thrombotic surface. A reduction of platelet accumulation on the coated surface is observed in the *single-* or *dual-layer* stent cases when compared to a non-stented *reference* chamber (see Fig. 5A). This result is confirmed by a quantification showing a 28% and 41% reduction in thrombus area for the *single-* and *dual-layer* stents respectively when compared to *reference* chamber coated with HAP, even though statistical significance was only reached with the *single-layer* stent (*reference* HAP: $35.3 \pm 3.7\%$; *single-layer* stent: $25.5 \pm 3.5\%$; *dual-layer* stent: $21 \pm 5.4\%$; $p = 0.0595$) (see Fig. 5B). In summary, the results indicate that the presence of a stent, regardless of its geometry, reduces thrombus formation in a chamber coated with thrombogenic material. Except for qualitative differences in aggregate coverage distribution, the two stent designs exhibit no significant difference in total aggregate size.

3.2. In silico results

The continuum fluid simulations of the entire vessel segment reveal the influence of the implanted stents on the local flow profiles in vicinity to the wall. While the three setups – non-stented *reference*, *single-layer* and *dual-layer* stent – are configured with the same flow rate, they display a different average local velocity 250 μm from the wall of 72.7 mm/s, 59.4 mm/s and 43.9 mm/s, respectively. The standard deviations are insignificant (see average 1D radial flow profiles in Fig. 13).

The different local velocities are subsequently applied as velocity boundary conditions in the configurations of the cellular flow simulations. The respective boundaries are located at the same distance of

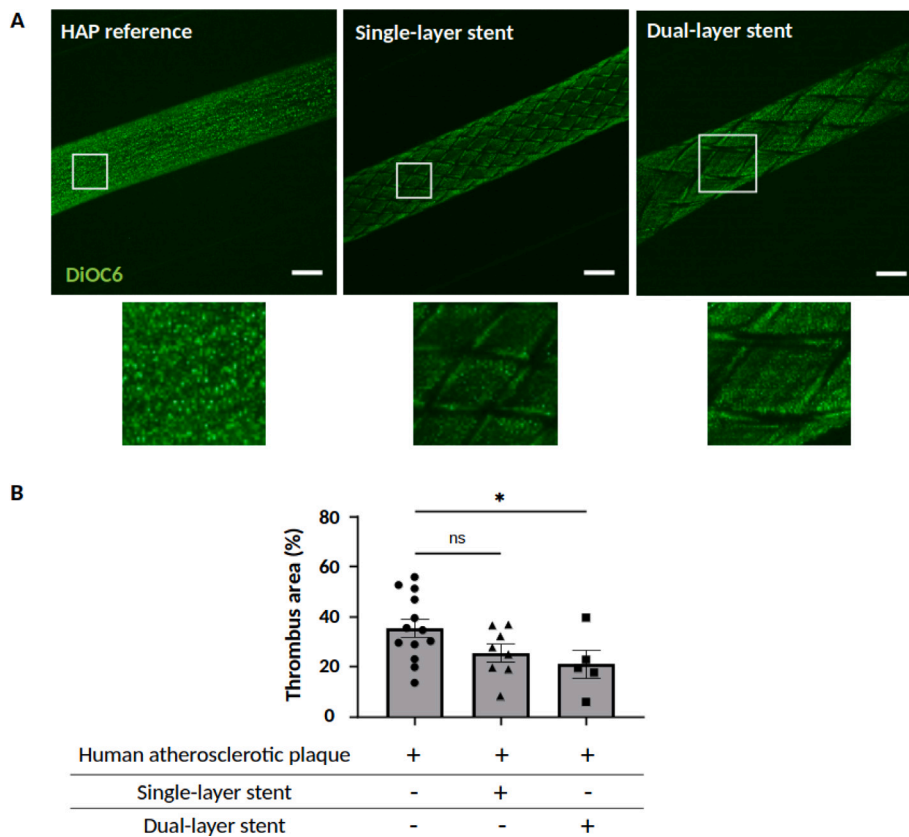


Fig. 5. Images of platelet aggregates on stents and human atherosclerotic plaque (HAP). (A) Platelet aggregation on HAP in the *reference* chamber (no stent) (left), in a chamber implanted with a *single-layer* (middle) and a *dual-layer* (right) carotid stent, after 10 min perfusion of anticoagulated whole blood labelled with DiOC₆. Scale bar: 2 mm. (B) Surface area quantification of platelet aggregation in the *reference* chamber coated only with HAP, or implanted with a *single-* or *dual-layer* stent (**p* = 0.0337; nsp = 0.0833). Values are the mean ± standard error of the mean.

250 μm from the wall and drive the simulation of each case to reach 1 s of simulated flow (see Movies 16 to 18). Following the completion of the simulations, the local flow dynamics and cellular distributions are analysed and compared.

Fig. 6A and B shows the shear rate profile for the *single-* and *dual-layer* stent case, respectively. Both cases display the highest shear rate magnitude at the topmost point of the innermost strut, at a Z-axis height of 135 μm for the large strut and 166.5 μm for the small inner layer strut. Peak shear rate values reach 1810 s⁻¹ for the *single-layer* case and 2236 s⁻¹ for the *dual-layer* case. The peak rate of elongation values of 490 s⁻¹ and 721 s⁻¹ for the *single-* and *dual-layer* case respectively, are located slightly below the topmost strut point towards the proximal and distal side (see Fig. 7).

Although the set surface velocity in the *dual-layer* case is 26% lower than in the *single-layer* case, the addition of the inner layer strut increases the peak shear rate by 24% and rate of elongation by 47%. In comparison, the *reference* case experiences a maximum shear rate of 545 s⁻¹ and peak rate of elongation values of 113 s⁻¹ at a faster flow velocity. The peak shear rate represents the wall shear rate at a Z-axis height of 0 μm. The existence of elongational flows in the non-stented channel altogether can be contributed to sites of cell - cell interactions, since on the macroscale that flow is comprised of pure shear.

The velocity profiles of the *single-* and *dual-layer* case are visualized in the form of streamlines superimposed on a side-view visualization of the simulations in Figs. 8 and 9, respectively. The *single-layer* case displays a higher flow velocity throughout the channel, due to the higher velocity computed from the whole-stent macroscale simulations. Additionally, the inner layer of the *dual-layer* design forces the velocity gradient towards the top plane of the domain, which correlates with the elevated shear and elongational flow depicted in Figs. 6(B) and 7(B). The *single-layer* case exhibits significant recirculation regions spanning

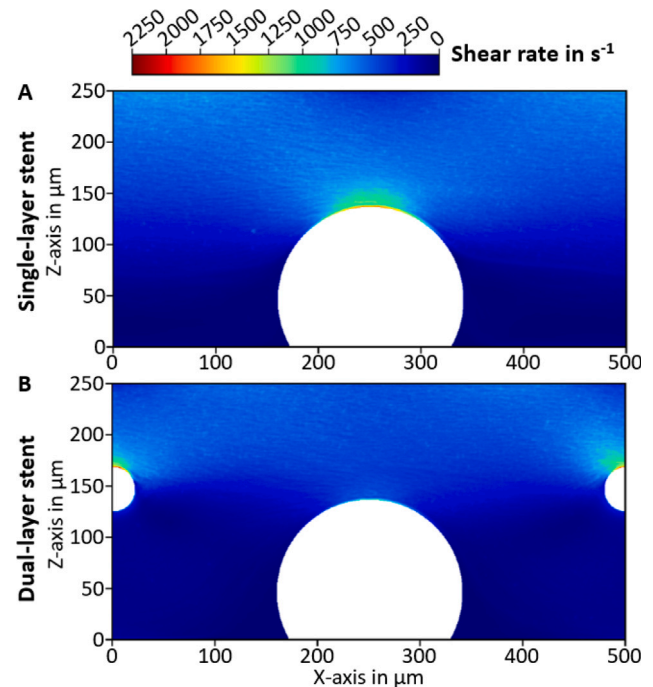


Fig. 6. Average shear rate profile in cell-resolved simulation for (A) *single-layer* and (B) *dual-layer* case with flow in positive X-direction. Results are averaged across the Y-axis and over multiple time steps.

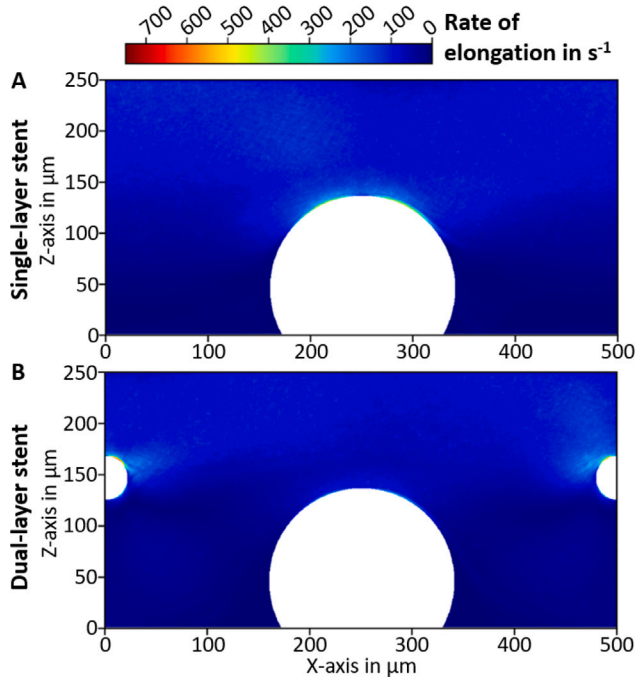


Fig. 7. Average rate of elongation profile in cell-resolved simulation for (A) *single-layer* and (B) *dual-layer* case with flow in positive X-direction. The velocity results are averaged across the Y-axis and over multiple time steps.

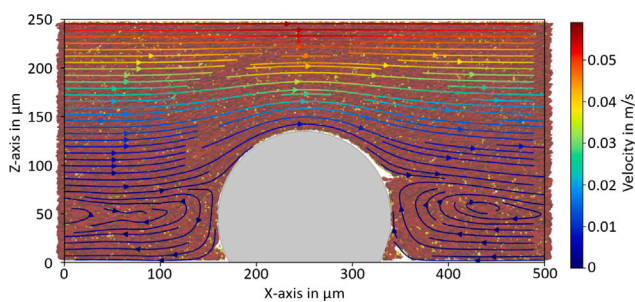


Fig. 8. Streamlines coloured by average velocity superimposed on side-view visualization of the *single-layer* stent case. The velocity results are averaged across the Y-axis and over multiple time steps and the cell positions are captured at the final time step $t = 1$ s. The visible RBCs and platelets are coloured in dark red and yellow, respectively.

across the bottom plane of the channel, proximal and distal from the stent strut location. The flow separation occurs on the distal side of the stent strut at an approximate Z-axis height of $85 \mu\text{m}$, while the reattachment on the proximal strut side is situated slightly lower at about $75 \mu\text{m}$. Additionally, small stagnation zones appear at the bottom plane of the domain, ranging approximately $20 \mu\text{m}$ in negative and positive X-direction from the proximal and distal strut intersection points, respectively.

The *dual-layer* design displays smaller separated flow regions, occurring around $75 \mu\text{m}$ before and after the large stent strut intersection on the X-axis and at a Z-axis height of approximately $70 \mu\text{m}$ on both sides of the large strut. These regions are not fully recirculating and can be considered stagnation zones, due to the very low local velocities (below 0.0001 mm/s). Naturally, the *reference* case does not display recirculation regions or stagnation zones.

Observation of the underlying side-view visualizations suggests a correlation between the location and size of the separated flow regions and the cellular distributions: the flow separation points align with volumes of low RBC concentration and platelet accumulation in both the *single-* and *dual-layer* design. These volumes are well visible in Figs. 8 and 9 in white colour. The largest volume appears at the distal flow separation point of the large strut for both cases.

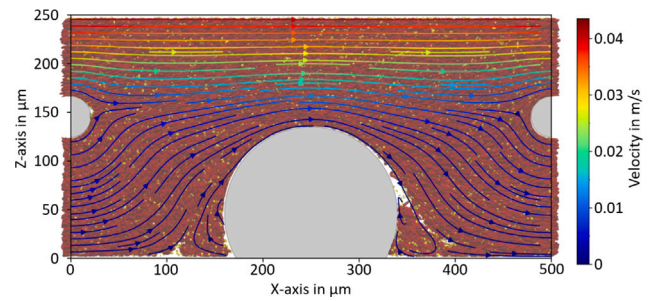


Fig. 9. Streamlines coloured by average velocity superimposed on side-view visualization of the *dual-layer* stent case. The velocity results are averaged across the Y-axis and over multiple time steps and the cell positions are captured at the final time step $t = 1$ s. The visible RBCs and platelets are coloured in dark red and yellow, respectively.

To confirm and quantify differences in cellular distribution, the average cell volume concentrations are evaluated in Fig. 10. The *reference* case displays almost homogeneous hematocrit and platelet volume concentration distribution, matching the initialized concentrations of 25% and 1.7%, respectively (see Fig. 10A and D). Deviations can be seen in the volume layer close to the vessel wall: a reduced hematocrit concentration and an increased platelet volume concentration at the vessel wall are physiologically expected due to the shear-induced formation of a cell free layer and subsequent margination of platelets into this layer [63,72].

The previously observed recirculation regions in the *single-layer* case are reflected in the layered cell distributions (see Fig. 10B and E). The flow separation interface creates a layer of reduced hematocrit concentration, which is largest at the distal stent strut separation point. The same area exhibits increased platelet concentration. The stagnation zones at the proximal and distal strut intersection with the bottom plane also display low RBC concentration and increased platelet concentration.

The *dual-layer* design (see Fig. 10C and F) shows the absence of recirculation regions. The previously observed stagnation zones contain accumulations of RBCs and platelets in comparison to the surrounding concentrations. Their classification as stagnation zones is further substantiated by the comparatively low flow velocity, that also leads to lower standard deviation in cell concentration (see Fig. 14 C and F). The similar regions of reduced RBC concentration and increased platelet concentration as observed in the *single-layer* case can be seen at the flow separation interface of the *dual-layer* case. The inner layer strut exhibits an increase in platelet concentration on the distal side and a layer of reduced RBC concentration spanning across the domain in X-direction.

To display platelet availability at the vessel wall where initial adhesion and aggregation commonly occurs [32], the platelet concentration in $4 \mu\text{m}$ distance to the wall is evaluated along the X-axis of the domains (see Fig. 11). These are the platelets assumed to be available for binding at the wall. In alignment with previous results, the *reference* case displays an even distribution at around 1%. Both stent cases show highly uneven platelet availability across the surface. While both designs display peak concentrations proximal and distal to the large strut location, the *dual-layer* case exhibits increased platelet concentration below the inner layer strut, when compared to the *single-layer* case. The concentration peaks in the *dual-layer* design match the location of platelet accumulations in the stagnation zones, seen in Fig. 10F. The distal concentration peak in the *single-layer* case is an accumulation point located within the stagnation zone, as well. The discontinuity in concentration before and after the accumulation points can be attributed to low local platelet occurrence that is represented as zero by the discrete data-saving steps of the evaluated time range.

Fig. 12A combines the total average platelet concentration within $4 \mu\text{m}$ distance to the vessel wall for each case. Both stented cases display lower platelet concentration than the *reference* case at 2.19%, with

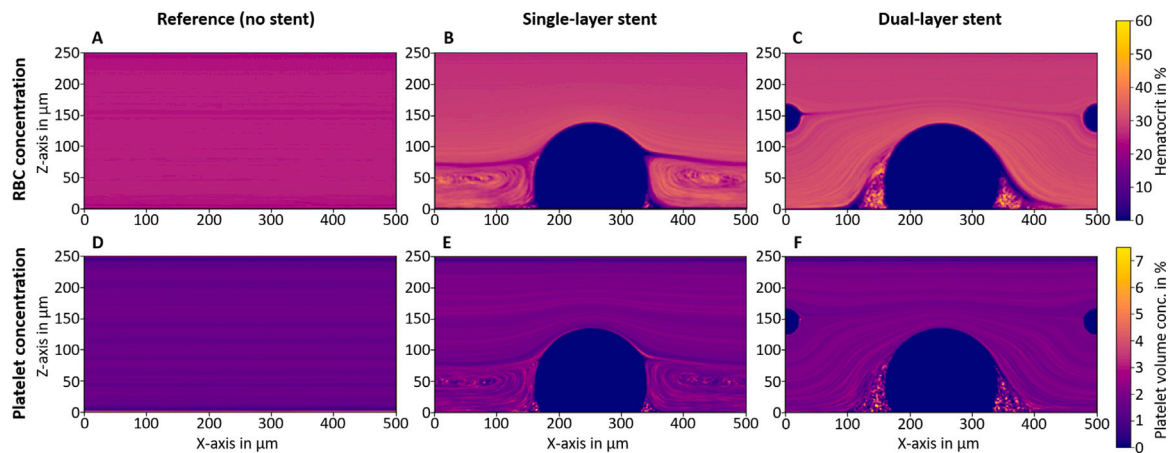


Fig. 10. Average cell volume concentration across X- and Z-axis for the (A & D) *reference* (no stent), (B & E) *single-layer* and (C & F) *dual-layer* stent, respectively. RBC concentration in top row (A - C) and platelet concentration in bottom row (D - F). Results are averaged across the Y-axis and over multiple time steps. Flow is driven in positive X-direction.

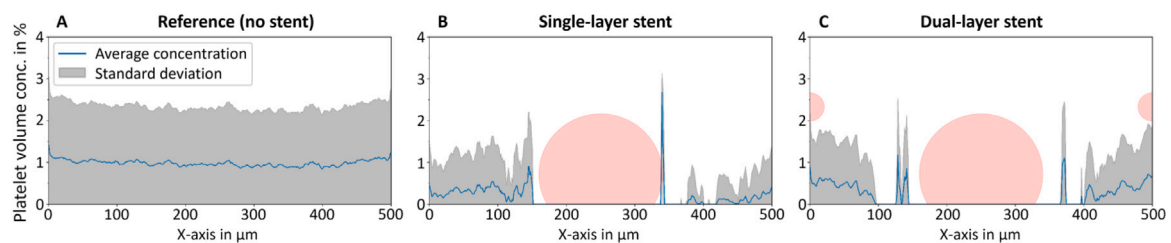


Fig. 11. Platelet volume concentration within 4 μm distance to the vessel wall for the (A) *reference* (no stent), (B) *single-layer* and (C) *dual-layer* stent, respectively. The local volume concentration is time averaged between 0.5–1 s of simulated flow. Flow is driven in positive X-direction. As a visual indicator, the stent strut locations are marked in red in B and C. Note: the Y-axis represents platelet concentration and not spatial scale.

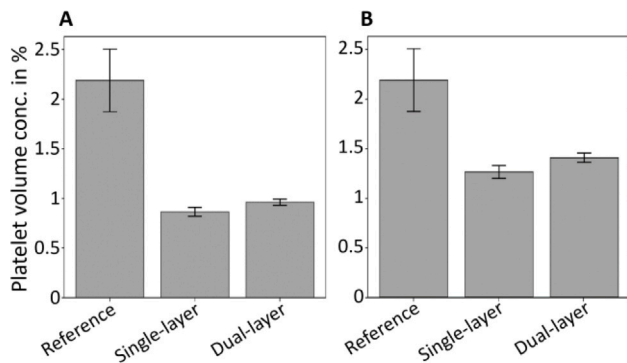


Fig. 12. Total average platelet concentration within 4 μm distance to the vessel wall, Without (A) and with (B) normalizing for the fluid volume. Normalization excludes the empty volume of the large stent strut circular segment, between 0 and 4 μm from the wall. Results are time-averaged.

0.86% for the *single-layer* and 0.96% for the *dual-layer* design. Note that these values are based on the total volume, irrespective of the volume exclusion of the stents. Considering fluid-only volume (see Fig. 12B) leads to the concentrations of 1.26% and 1.41% for the *single-* and *dual-layer* case, respectively. The difference between both stented cases remains small, but significant when taking the standard deviation into account. The trend of the results qualitatively matches the experimental platelet surface coverage measurements in Figs. 4 and 5B.

4. Discussion

In this study, a *single-layer* and a *dual-layer* carotid stent design were investigated by utilizing a novel macrofluidic carotid chamber for platelet surface coverage measurements and a multiscale simulation

setup to study flow dynamics and cellular distributions in vicinity to the vessel wall.

The multiscale setup consists of macroscale continuum CFD simulations of the entire stented segment to accurately inform the local velocity boundaries for microscale cell-resolved simulations, capturing the dynamics around individual struts. The differences in local flow velocity revealed by the macroscale simulations and the heterogeneous cellular distributions discovered by the microscale simulations substantiate the need for a multiscale simulation setup to study stent design in large vessels.

Both stent designs display a decreased platelet surface coverage in comparison to non-stented *reference* experiments (see Figs. 4 and 5). Two separate coatings were used: collagen coating (see Fig. 4), representing the exposure following endothelial damage, and HAP homogenate (see Fig. 5) to mimic the presence of atherosclerotic plaque. While HAP homogenate more closely resembles a ruptured plaque than fibrillar collagen coming from equine or bovine tendons, it has to be noted that the used plaque is crushed, thus the integrity of the collagen fibres and other proteins is likely impaired. Nonetheless, the experimentally observed reduction in platelet coverage of the vessel surface for both collagen and HAP covered surfaces could be the result of reduced near-wall platelet availability as found in the simulations. This is confirmed by evaluation of the cellular simulations: the trend in local platelet availability in close vicinity to the vessel wall (see Fig. 12) qualitatively matches the difference in experimental platelet coverage. It can be concluded, that the introduction of flow obstructions in the form of stent struts in a stented vessel segment reduces local platelet availability and subsequently the likelihood of aggregation to highly thrombogenic exposed collagen and HAP.

The simulations further reveal a significant difference in shear rate and rate of elongation between the *reference*, *single-layer* and *dual-layer* stent case (see Figs. 6 and 7). The latter, although driven by the lowest velocity boundary condition, exhibits the largest peaks in both

shear rate ($>2200\text{ s}^{-1}$) and rate of elongation ($>700\text{ s}^{-1}$). The shear rate is well within the range where immobilized VWF can unfold and expose the A1 domain ($>1000\text{ s}^{-1}$), while it stays below pathologic levels associated with shear-induced platelet aggregation [31,73,74]. The rate of elongation on the other hand exceeds the critical range of $300\text{--}600\text{ s}^{-1}$ defined by Sing et al. to be sufficient for the unfolding of plasma suspended VWF molecules [75]. Unfolded VWF molecules mediate the adhesion and aggregation of platelets, which is the initial facilitator of thrombus formation in arterial thrombosis [32,76].

In alignment with previous findings by Jiménez et al., large recirculation regions spanning the whole distance between neighbouring stent struts are demonstrated in the *single-layer* stent design [34]. In contrast to this, the *dual-layer* design is characterized by stagnation zones on the proximal and distal side of the large outer layer stent strut and the absence of recirculation regions. Flow stagnation is associated with blood coagulation and thrombosis, most commonly the formation of RBC rich clots in venous thrombosis. The increased RBC concentration within the stagnation zones of the *dual-layer* stent case therefore further heightens the likelihood of coagulation-driven clot formation [77,78]. Additionally, the *dual-layer* design displays higher platelet concentration in close vicinity to the vessel wall compared to the *single-layer* design (see Fig. 12). This higher platelet availability translates to an increased probability of contact between platelets and thrombogenic material and is associated with a higher risk for thrombotic complications [79,80]. To summarize, the presence of stagnation zones, heightened shear flow, including elongational flow, and increased platelet concentration are observed in the *dual-layer* design in comparison to the *single-layer* design. While not observed experimentally here, this confirms and gives a possible explanation for the results of recent studies by Yilmaz et al. and Sykora et al., that *dual-layer* stents are potentially more thrombogenic than *single-layer* stents [26,27]. The findings require further confirmation through simulations and experiments. Subsequent platelet surface coverage measurements in the presented carotid chamber with a less thrombogenic coating could reveal further trends for thrombus formation in the environment of a *dual-layer* stented carotid artery.

In general, the findings highlight that even minor differences in the local environment, introduced by the inner layer of the *dual-layer* stent, significantly influence factors that might be associated with ST, such as shear flow magnitude, flow stagnation zones, and platelet availability. Notably, the presence, shape and magnitude of the recirculation regions and stagnation zones, observable in cost-effective continuum flow simulations, substantially impact the cellular distributions. These insights establish the potential to further optimize carotid stent design, as well as vascular stent design in general. The correlation between recirculation regions and cell distributions suggests that simple continuum CFD simulations can provide valuable knowledge about cellular distributions. Figure 15 confirms that the same streamline profiles resulting from the cellular simulations can be recreated by computationally less demanding CFD simulations, which could reduce execution time and cost to be more in line with the less complex methods currently used in stent design studies [34,39,40]. Additional simulations in the presented multiscale setup have to be deployed to quantify the described interdependence of recirculation regions and cellular distributions. A parametric study can subsequently assess strut shape, size and alignment as well as embedment depth to optimize the overall stent design towards creating physiological and therefore favourable flow magnitudes and cellular distributions.

4.1. Limitations and future work

Future work on the comparison between *single-layer* and *dual-layer* carotid stents includes assessing local differences in platelet coverage across the stent struts and free cell areas in more detail. Observations of the platelet thrombi surface on the fluorescent microscope images and simulated platelet concentration distributions show differences between the *single-* and *dual-layer* design, but additional experiments and

simulations are required to quantify the emergent trend. Furthermore, the influence of different flow velocities, hematocrit concentrations and RBC stiffness on platelet coverage and availability, can be assessed in future experiments and simulations [63,81].

To improve the accuracy of the simulations, a two-way coupling of the presented multiscale framework could be considered. The current simulation setup can be further improved by including pulsatility, vessel wall elasticity and stent strut braiding to more closely resemble *in vitro* as well as *in vivo* conditions. To further approximate the latter, patient-specific anomalies of diseased vessels, such as narrowing of the lumen or a stiffened vessel wall, can be included in the geometry of the current setup. Advancing the cellular simulation framework to actively model accurate platelet binding behaviour [69] could assist in studying ST risk in varying stent designs.

5. Conclusion

In summary, a comparison between a *single-layer* and a *dual-layer* stent intended for CAS in a combined *in vitro* and *in silico* setup is presented. The results indicate the presence of high elongational flows in combination with an increased platelet availability and local stagnation zones in the recently introduced *dual-layer* carotid stent design in comparison to the more established *single-layer* design. Additional experiments are required to validate the findings.

Furthermore, a significant influence of stent strut recirculation regions on local cell distributions is revealed by the simulations. This facilitates a novel approach to optimize stent design in general towards creating a favourable cellular flow environment around the stent struts.

CRediT authorship contribution statement

Christian J. Spieker: Writing – review & editing, Writing – original draft, Visualization, Validation, Methodology, Investigation, Formal analysis, Data curation, Conceptualization. **Axelle Y. Kern:** Writing – review & editing, Writing – original draft, Visualization, Validation, Methodology, Investigation, Formal analysis, Data curation, Conceptualization. **Netanel Korin:** Writing – review & editing, Conceptualization. **Pierre H. Mangin:** Writing – review & editing, Supervision, Resources, Project administration, Formal analysis, Conceptualization. **Alfons G. Hoekstra:** Writing – review & editing, Methodology, Conceptualization. **Gábor Závodszy:** Writing – review & editing, Supervision, Software, Resources, Project administration, Formal analysis, Conceptualization.

Declaration of competing interest

The authors declare that they have no known competing financial interests or personal relationships that could have appeared to influence the work reported in this paper.

Acknowledgments

C.J.S., A.G.H. and G.Z. acknowledge financial support by the European Union Horizon 2020 research and innovation programme under Grant Agreement No. 823712, the CompBioMed2 Project. C.J.S., A.G.H. and G.Z. are funded by CompBioMed2. The use of supercomputer facilities in this work was sponsored by NWO Exacte Wetenschappen (Physical Sciences). The authors would like to thank Joey van der Kaaij, David de Kanter, and Robert Belleman for their contributions to the development of the visualization used in Fig. 3 and the animations displayed in Supplementary Movies S1 to S3.

Appendix A. Supplementary data

Supplementary material related to this article can be found online at <https://doi.org/10.1016/j.combiomed.2024.109313>.

References

- [1] M.L. Flaherty, B. Kissela, J.C. Khoury, K. Alwell, C.J. Moomaw, D. Woo, P. Khatri, S. Ferioli, O. Adeoye, J.P. Broderick, D. Kleindorfer, Carotid artery stenosis as a cause of stroke, *Neuroepidemiology* 40 (1) (2012) 36–41, <http://dx.doi.org/10.1159/000341410>.
- [2] J. Iqbal, J. Gunn, P.W. Serruys, Coronary stents: historical development, current status and future directions, *Br. Med. Bull.* 106 (1) (2013) 193–211, <http://dx.doi.org/10.1093/bmb/ldt009>.
- [3] C.J. White, Carotid artery stenting, *J. Am. Coll. Cardiol.* 64 (7) (2014) 722–731, <http://dx.doi.org/10.1016/j.jacc.2014.04.069>.
- [4] R.A. Byrne, G.W. Stone, J. Ormiston, A. Kastrati, Coronary balloon angioplasty, stents, and scaffolds, *Lancet* 390 (10096) (2017) 781–792, [http://dx.doi.org/10.1016/s0140-6736\(17\)31927-x](http://dx.doi.org/10.1016/s0140-6736(17)31927-x).
- [5] Y. Gouffic, N.D. Schiava, F. Thaveau, E. Rosset, J.-P. Favre, L.S. du Mont, J.-M. Alsac, R. Hassen-Khodja, T. Reix, E. Allaire, E. Ducasse, R. Soler, B. Guyomarc'h, B. Nasr, Stenting or surgery for de novo common femoral artery stenosis, *JACC: Cardiovasc. Interv.* 10 (13) (2017) 1344–1354, <http://dx.doi.org/10.1016/j.jcin.2017.03.046>.
- [6] J.H. Lichtman, M.R. Jones, E.C. Leifheit, A.J. Sheffet, G. Howard, B.K. Lal, V.J. Howard, Y. Wang, J. Curtis, T.G. Brott, Carotid endarterectomy and carotid artery stenting in the US medicare population, 1999–2014, *JAMA* 318 (11) (2017) 1035, <http://dx.doi.org/10.1001/jama.2017.12882>.
- [7] E.E. de Vries, E.J. Vonken, L.J. Kappelle, R.J. Toorop, G.J. de Borst, Short-term double layer mesh stent patency for emergent or elective carotid artery stenting, *Stroke* 50 (7) (2019) 1898–1901, <http://dx.doi.org/10.1161/strokeaha.118.024586>.
- [8] A. Angelini, B. Reimers, M.D. Barbera, S. Saccà, G. Pasquetto, C. Cernetti, M. Valente, P. Pascotto, G. Thiene, Cerebral protection during carotid artery stenting, *Stroke* 33 (2) (2002) 456–461, <http://dx.doi.org/10.1161/hs0202.102337>.
- [9] J.A. Vos, Evidence overview: benefit of cerebral protection devices during carotid artery stenting, *J. Cardiovasc. Surg.* 58 (2) (2017) <http://dx.doi.org/10.23736/s0021-9509.16.09848-7>.
- [10] K.G. Moulakakis, S.N. Mylonas, A. Lazaris, G. Tsvigoulis, J. Kakis, G.S. Sfyroeras, C.N. Antonopoulos, E.N. Brountzos, S.N. Vasdekis, Acute carotid stent thrombosis, *Vasc. Endovascular Surg.* 50 (7) (2016) 511–521, <http://dx.doi.org/10.1177/1538574416665986>.
- [11] R. Pop, I. Zinchenko, V. Quenardelle, D. Mihoc, M. Manisor, J. Richter, F. Severac, R. Simu, S. Chibbaro, R. Gheoca, V. Quenardelle, O. Rouyer, V. Wolff, R. Beaujeux, Predictors and clinical impact of delayed stent thrombosis after thrombectomy for acute stroke with tandem lesions, *Am. J. Neuroradiol.* (2019) <http://dx.doi.org/10.3174/ajnr.a5976>.
- [12] A. Renú, J. Blasco, C. Laredo, L. Llull, X. Urrea, V. Obach, A. López-Rueda, S. Rudilosso, F. Zarco, E. González, J.D. Guio, S. Amaro, A. Chamorro, Carotid stent occlusion after emergent stenting in acute ischemic stroke: Incidence, predictors and clinical relevance, *Atherosclerosis* 313 (2020) 8–13, <http://dx.doi.org/10.1016/j.atherosclerosis.2020.09.002>.
- [13] R. Pop, A. Hasiu, P. Mangin, F. Severac, D. Mihoc, D. Nistoran, M. Manisor, M. Simu, S. Chibbaro, R. Gheoca, V. Quenardelle, O. Rouyer, V. Wolff, R. Beaujeux, Postprocedural antiplatelet treatment after emergent carotid stenting in tandem lesions stroke: Impact on stent patency beyond day 1, *Am. J. Neuroradiol.* 42 (5) (2021) 921–925, <http://dx.doi.org/10.3174/ajnr.a6993>.
- [14] E. Spronk, G. Sykes, S. Falcione, D. Munsterman, T. Joy, J. Kamtchum-Tatuene, G.C. Jickling, Hemorrhagic transformation in ischemic stroke and the role of inflammation, *Front. Neurol.* 12 (2021) <http://dx.doi.org/10.3389/fneur.2021.661955>.
- [15] D.E. Cutlip, D.S. Baim, K.K.L. Ho, J.J. Popma, A.J. Lansky, D.J. Cohen, J.P. Carrozza, M.S. Chauhan, O. Rodriguez, R.E. Kuntz, Stent thrombosis in the modern era, *Circulation* 103 (15) (2001) 1967–1971, <http://dx.doi.org/10.1161/01.cir.103.15.1967>.
- [16] T. Palmerini, G. Biondi-Zoccai, D.D. Riva, A. Mariani, P. Genereux, A. Branzi, G.W. Stone, Stent thrombosis with drug-eluting stents, *J. Am. Coll. Cardiol.* 62 (21) (2013) 1915–1921, <http://dx.doi.org/10.1016/j.jacc.2013.08.725>.
- [17] M. Gopalakrishnan, A. Lotfi, Stent thrombosis, *Semin. Thromb. Hemost.* 44 (01) (2017) 046–051, <http://dx.doi.org/10.1055/s-0037-1606178>.
- [18] J. Torrado, L. Buckley, A. Durán, P. Trujillo, S. Toldo, J.V. Raleigh, A. Abbate, G. Biondi-Zoccai, L.A. Guzmán, Restenosis, stent thrombosis, and bleeding complications, *J. Am. Coll. Cardiol.* 71 (15) (2018) 1676–1695, <http://dx.doi.org/10.1016/j.jacc.2018.02.023>.
- [19] R. Virmani, G. Guagliumi, A. Farb, G. Musumeci, N. Grieco, T. Motta, L. Mihalec, M. Tsepili, O. Valsecchi, F.D. Kolodgie, Localized hypersensitivity and late coronary thrombosis secondary to a sirolimus-eluting stent, *Circulation* 109 (6) (2004) 701–705, <http://dx.doi.org/10.1161/01.cir.0000116202.41966.d4>.
- [20] S.-H. Kang, I.-H. Chae, J.-J. Park, H.S. Lee, D.-Y. Kang, S.-S. Hwang, T.-J. Youn, H.-S. Kim, Stent thrombosis with drug-eluting stents and bioresorbable scaffolds, *JACC: Cardiovasc. Interv.* 9 (12) (2016) 1203–1212, <http://dx.doi.org/10.1016/j.jcin.2016.03.038>.
- [21] N. Foin, S. Lu, J. Ng, H. Bulluck, D. Hausenloy, P. Wong, R. Virmani, M. Joner, Stent malapposition and the risk of stent thrombosis: mechanistic insights from an in vitro model, *EuroIntervention* 13 (9) (2017) e1096–e1098, <http://dx.doi.org/10.4244/eij-d-17-00381>.
- [22] J.A.R. Pfaff, C. Maurer, E. Broussalis, H. Janssen, R. Blanc, C. Dargazanli, V. Costalat, M. Piotin, F. Runck, A. Berlis, M. Killer-Oberpfalzer, J.T. Hensler, M. Bendszus, F. Wodarg, M.A. Möhlenbruch, Acute thromboses and occlusions of dual layer carotid stents in endovascular treatment of tandem occlusions, *J. NeuroInterventional Surg.* 12 (1) (2019) 33–37, <http://dx.doi.org/10.1136/neurintsurg-2019-015032>.
- [23] T. Klail, C. Kurmann, J. Kaesmacher, A. Mujanovic, E.I. Piechowski, T. Dobrocky, S. Pilgram-Pastor, A. Scutelnic, M.R. Heldner, J. Gralla, P. Mordasini, Safety and efficacy of carotid artery stenting with the CGuard double-layer stent in acute ischemic stroke, *Clin. Neuroradiol.* 33 (1) (2022) 237–244, <http://dx.doi.org/10.1007/s00062-022-01209-3>.
- [24] O. Diaz, G. Lopez, J.O.F. Roehm, G.D. la Rosa, F. Orozco, R. Almeida, The Casper carotid artery stent: a unique all metal micromesh stent designed to prevent embolic release, *J. NeuroInterventional Surg.* 10 (2) (2017) 133–136, <http://dx.doi.org/10.1136/neurintsurg-2016-012913>.
- [25] L. Capoccia, P. Sirignano, W. Mansour, A. d'Adamo, E. Sbarigia, P. Mariani, C. Di Biasi, F. Speziale, Peri-procedural brain lesions prevention in CAS (3PCAS): Randomized trial comparing CGuard™ stent vs. Wallstent™, *Int. J. Cardiol.* 279 (2019) 148–153, <http://dx.doi.org/10.1016/j.ijcard.2018.09.066>.
- [26] U. Yilmaz, H. Körner, R. Mühl-Benninghaus, A. Simgen, C. Kraus, S. Walter, S. Behnke, K. Faßbender, W. Reith, M.M. Unger, Acute occlusions of dual-layer carotid stents after endovascular emergency treatment of tandem lesions, *Stroke* 48 (8) (2017) 2171–2175, <http://dx.doi.org/10.1161/strokeaha.116.015965>.
- [27] J. Sýkora, K. Zelenák, M. Vorčák, M. Števík, M. Sýkora, J. Sívák, M. Rovniák, J. Zapletalová, J. Mužík, I. Šinák, E. Kurča, L. Kerev, J. Fiehler, Comparison of restenosis risk in single-layer versus dual-layer carotid stents: A duplex ultrasound evaluation, *Cardiovasc. Intervent. Radiol.* 45 (9) (2022) 1257–1266, <http://dx.doi.org/10.1007/s00270-022-03200-4>.
- [28] K. Nishihira, A. Yamashita, T. Ishikawa, K. Hatakeyama, Y. Shibata, Y. Asada, Composition of thrombi in late drug-eluting stent thrombosis versus de novo acute myocardial infarction, *Thromb. Res.* 126 (3) (2010) 254–257, <http://dx.doi.org/10.1016/j.thromres.2009.11.010>.
- [29] M. Sadowski, M. Ząbczyk, A. Undas, Coronary thrombus composition: Links with inflammation, platelet and endothelial markers, *Atherosclerosis* 237 (2) (2014) 555–561, <http://dx.doi.org/10.1016/j.atherosclerosis.2014.10.020>.
- [30] J. Riegger, R.A. Byrne, M. Joner, S. Chandraratne, A.H. Gershlick, J.M. ten Berg, T. Adriaenssens, G. Guagliumi, T.C. Godschalk, F.-J. Neumann, D. Trenk, L.J. Feldman, P.G. Steg, W. Desmet, F. Alfonso, A.H. Goodall, R. Wojdyła, D. Dudek, V. Philipp, S. Opinaldo, A. Titova, N. Malik, J. Cotton, D.A. Jhagroe, A.A. Heestermaers, P. Sinnaeve, P. Vermeersch, C. Valina, C. Schulz, A. Kastrati, S. Massberg, Histopathological evaluation of thrombus in patients presenting with stent thrombosis. A multicenter European study: a report of the prevention of late stent thrombosis by an interdisciplinary global European effort consortium, *Eur. Heart J.* 37 (19) (2015) 1538.1–1549, <http://dx.doi.org/10.1093/eurheartj/ehv419>.
- [31] Z.L. Liu, D.N. Ku, C.K. Aidun, Mechanobiology of shear-induced platelet aggregation leading to occlusive arterial thrombosis: A multiscale in silico analysis, *J. Biomech.* 120 (2021) 110349, <http://dx.doi.org/10.1016/j.jbiomech.2021.110349>.
- [32] D.A. Kim, D.N. Ku, Structure of shear-induced platelet aggregated clot formed in an in vitro arterial thrombosis model, *Blood Adv.* 6 (9) (2022) 2872–2883, <http://dx.doi.org/10.1182/bloodadvances.2021006248>.
- [33] A.O. Frank, P.W. Walsh, J.E. Moore, Computational fluid dynamics and stent design, *Artif. Organs.* 26 (7) (2002) 614–621, <http://dx.doi.org/10.1046/j.1525-1594.2002.07084.x>.
- [34] J.M. Jiménez, P.F. Davies, Hemodynamically driven stent strut design, *Ann. Biomed. Eng.* 37 (8) (2009) 1483–1494, <http://dx.doi.org/10.1007/s10439-009-9719-9>.
- [35] F.J. Gijsen, F. Migliva, S. Schievano, L. Succi, L. Petrini, A. Thury, J.J. Wentzel, A.F. van der Steen, P.W. Serruys, G. Dubini, Simulation of stent deployment in a realistic human coronary artery, *BioMed. Eng. Online* 7 (1) (2008) 23, <http://dx.doi.org/10.1186/1475-925x-7-23>.
- [36] D. Evans, P. Lawford, J. Gunn, D. Walker, D. Hose, R. Smallwood, B. Chopard, M. Krafczyk, J. Bernsdorf, A. Hoekstra, The application of multiscale modelling to the process of development and prevention of stenosis in a stented coronary artery, *Phil. Trans. R. Soc. A* 366 (1879) (2008) 3343–3360, <http://dx.doi.org/10.1098/rsta.2008.0081>.
- [37] A. Caiazzo, D. Evans, J.-L. Falcone, J. Hegewald, E. Lorenz, B. Stahl, D. Wang, J. Bernsdorf, B. Chopard, J. Gunn, R. Hose, M. Krafczyk, P. Lawford, R. Smallwood, D. Walker, A. Hoekstra, A complex automata approach for in-stent restenosis: Two-dimensional multiscale modelling and simulations, *J. Comput. Sci.* 2 (1) (2011) 9–17, <http://dx.doi.org/10.1016/j.jocs.2010.09.002>.
- [38] P.S. Zun, T. Anikina, A. Svitenkov, A.G. Hoekstra, A comparison of fully-coupled 3D in-stent restenosis simulations to in-vivo data, *J. Endovasc. Ther.* 8 (2017) <http://dx.doi.org/10.3389/fphys.2017.00284>.
- [39] J.K. Chesnutt, H.-C. Han, Simulation of the microscopic process during initiation of stent thrombosis, *Comput. Biol. Med.* 56 (2015) 182–191, <http://dx.doi.org/10.1016/j.compbiomed.2014.11.006>.
- [40] J.K.W. Chesnutt, H.-C. Han, Computational simulation of platelet interactions in the initiation of stent thrombosis due to stent malapposition, *Phys. Biol.* 13 (1) (2016) 016001, <http://dx.doi.org/10.1088/1478-3975/13/1/016001>.

- [41] A.Y. Kern, Y. Kreinin, L. Charle, M. Epshteyn, N. Korin, P.H. Mangin, A macrofluidic model to investigate the intrinsic thrombogenicity of clinically used stents and develop less thrombogenic stents, *Heliyon* 10 (5) (2024) e26550, <http://dx.doi.org/10.1016/j.heliyon.2024.e26550>.
- [42] J. Krejza, M. Arkuszewski, S.E. Kasner, J. Weigle, A. Ustymowicz, R.W. Hurst, B.L. Cucchiara, S.R. Messe, Carotid artery diameter in men and women and the relation to body and neck size, *Stroke* 37 (4) (2006) 1103–1105, <http://dx.doi.org/10.1161/01.str.0000206440.48756.f7>.
- [43] A. Benetos, A. Simon, J. Levenson, P. Lagneau, J. Bouthier, M. Safar, Pulsed Doppler: an evaluation of diameter, blood velocity and blood flow of the common carotid artery in patients with isolated unilateral stenosis of the internal carotid artery, *Stroke* 16 (6) (1985) 969–972, <http://dx.doi.org/10.1161/01.str.16.6.969>.
- [44] M.F.A. Karel, T.P. Lemmens, B.M.E. Tullemans, S.J.H. Wielders, E. Gubbins, D. van Beurden, S. van Rijt, J.M.E.M. Cosemann, Characterization of atherosclerotic plaque coating for thrombosis microfluidics assays, *Cell. Mol. Bioeng.* 15 (1) (2021) 55–65, <http://dx.doi.org/10.1007/s12195-021-00713-9>.
- [45] C. Wissgott, W. Schmidt, C. Brandt, P. Behrens, R. Andresen, Preliminary clinical results and mechanical behavior of a new double-layer carotid stent, *J. Endovasc. Ther.* 22 (4) (2015) 634–639, <http://dx.doi.org/10.1177/1526602815593490>.
- [46] P. Montorsi, L. Caputi, S. Galli, P.M. Ravagnani, G. Teruzzi, A. Annoni, G. Calligaris, F. Fabbicocchi, D. Trabattoni, S. de Martini, L. Grancini, G. Pontone, D. Andreini, S. Troiano, D. Restelli, A.L. Bartorelli, Carotid wallstent versus road-saver stent and distal versus proximal protection on cerebral microembolization during carotid artery stenting, *JACC: Cardiovasc. Interv.* 13 (4) (2020) 403–414, <http://dx.doi.org/10.1016/j.jcin.2019.09.007>.
- [47] P.M. Knupp, Algebraic mesh quality metrics, *SIAM J. Sci. Comput.* 23 (1) (2001) 193–218, <http://dx.doi.org/10.1137/s1064827500371499>.
- [48] P. Knupp, Introducing the target-matrix paradigm for mesh optimization via node-movement, *Eng. Comput.* 28 (4) (2011) 419–429, <http://dx.doi.org/10.1007/s00366-011-0230-1>.
- [49] J. Tanigawa, P. Barlis, K. Dimopoulos, M. Dalby, P. Moore, C. Di Mario, The influence of strut thickness and cell design on immediate apposition of drug-eluting stents assessed by optical coherence tomography, *Int. J. Cardiol.* 134 (2) (2009) 180–188, <http://dx.doi.org/10.1016/j.ijcard.2008.05.069>.
- [50] S. Tabakova, E. Nikolova, S. Radev, Carreau model for oscillatory blood flow in a tube, in: *AIP Conference Proceedings*, AIP Publishing LLC, 2014, <http://dx.doi.org/10.1063/1.4902290>.
- [51] H.L. Goldsmith, V.T. Turitto, Rheological aspects of thrombosis and haemostasis: Basic principles and applications, *Thromb. Haemost.* 55 (03) (1986) 415–435, <http://dx.doi.org/10.1055/s-0038-1661576>.
- [52] L. Mountrakis, V. Azizi, G. Závodszy, Max, Jdebouter, AlekseyBelyaev, R. Joo-Kovacs, Alowayyed, C. Spieker, Erincorlez, MJdeHaan, Kostis Asteriou, UvaCsl/HemoCell: HemoCell v2.7, 2023, <http://dx.doi.org/10.5281/ZENODO.7713548>.
- [53] S. Chen, G.D. Doolen, Lattice boltzmann method for fluid flows, *Annu. Rev. Fluid Mech.* 30 (1) (1998) 329–364, <http://dx.doi.org/10.1146/annurev.fluid.30.1.329>.
- [54] T. Krüger, H. Kusumaatmaja, A. Kuzmin, O. Shardt, G. Silva, E.M. Viggen, *The Lattice Boltzmann Method: Principles and Practice*, Springer International Publishing, 2017, <http://dx.doi.org/10.1007/978-3-319-44649-3>.
- [55] J. Latt, O. Malaspinas, D. Kontaxakis, A. Parmigiani, D. Lagrava, F. Brogi, M.B. Belgacem, Y. Thorimbert, S. Leclaire, S. Li, F. Marson, J. Lemus, C. Kotsalos, R. Conradin, C. Coreixas, R. Petkantchin, F. Raynaud, J. Beny, B. Chopard, Palabos: Parallel lattice boltzmann solver, *Comput. Math. Appl.* 81 (2021) 334–350, <http://dx.doi.org/10.1016/j.camwa.2020.03.022>, URL: <https://www.sciencedirect.com/science/article/pii/S0898122120301267>.
- [56] P.L. Bhatnagar, E.P. Gross, M. Krook, A model for collision processes in gases. I. Small amplitude processes in charged and neutral one-component systems, *Phys. Rev.* 94 (3) (1954) 511–525, <http://dx.doi.org/10.1103/physrev.94.511>.
- [57] C.S. Peskin, The immersed boundary method, *Acta Numer.* 11 (2002) 479–517, <http://dx.doi.org/10.1017/s0962492902000077>.
- [58] L. Mountrakis, E. Lorenz, A.G. Hoekstra, Validation of an efficient two-dimensional model for dense suspensions of red blood cells, *Internat. J. Modern Phys. C* 25 (12) (2014) 1441005, <http://dx.doi.org/10.1142/s0129183114410058>.
- [59] L. Mountrakis, E. Lorenz, O. Malaspinas, S. Alowayyed, B. Chopard, A.G. Hoekstra, Parallel performance of an IB-LBM suspension simulation framework, *J. Comput. Sci.* 9 (2015) 45–50, <http://dx.doi.org/10.1016/j.jocs.2015.04.006>, URL: <https://www.sciencedirect.com/science/article/pii/S187750315000447>.
- [60] G. Závodszy, B. van Rooij, V. Azizi, A. Hoekstra, Cellular level in-silico modeling of blood rheology with an improved material model for red blood cells, *J. Endovasc. Ther.* 8 (AUG) (2017) <http://dx.doi.org/10.3389/fphys.2017.00563>.
- [61] C.J. Spieker, *Platelet Aggregation in Complex Vessel Geometries: An in Silico Study on Cellular Blood Flow Mechanics* (Ph.D. thesis), Universiteit van Amsterdam, 2024.
- [62] G. Závodszy, B. Van Rooij, V. Azizi, S. Alowayyed, A. Hoekstra, Hemocell: A high-performance microscopic cellular library, in: *Procedia Computer Science*, Vol. 108, Elsevier B.V., 2017, pp. 159–165, <http://dx.doi.org/10.1016/j.procs.2017.05.084>.
- [63] G. Závodszy, B. Van Rooij, B. Czaja, V. Azizi, D. De Kanter, A.G. Hoekstra, Red blood cell and platelet diffusivity and margination in the presence of cross-stream gradients in blood flows, *Phys. Fluids* 31 (3) (2019) <http://dx.doi.org/10.1063/1.5085881>.
- [64] B. Czaja, J. de Bouter, M. Heisler, G. Závodszy, S. Karst, M. Sarunic, D. Maberley, A. Hoekstra, The effect of stiffened diabetic red blood cells on wall shear stress in a reconstructed 3D microaneurysm, *Comput. Methods Biomech. Biomed. Eng.* 25 (15) (2022) 1691–1709, <http://dx.doi.org/10.1080/10255842.2022.2034794>.
- [65] B.J.M. van Rooij, G. Závodszy, A.G. Hoekstra, D.N. Ku, Biorheology of occlusive thrombi formation under high shear: in vitro growth and shrinkage, *Interface Focus* 10 (1) (2020) <http://dx.doi.org/10.1038/s41598-020-74518-7>.
- [66] B.J.M. van Rooij, G. Závodszy, A.G. Hoekstra, D.N. Ku, Haemodynamic flow conditions at the initiation of high-shear platelet aggregation: a combined in vitro and cellular in silico study, *Interface Focus* 11 (1) (2021) 20190126, <http://dx.doi.org/10.1098/rsfs.2019.0126>, URL: <https://royalsocietypublishing.org/doi/10.1098/rsfs.2019.0126>.
- [67] C.J. Spieker, G. Závodszy, C. Mouriaux, M. van der Kolk, C. Gachet, P.H. Mangin, A.G. Hoekstra, The effects of micro-vessel curvature induced elongational flows on platelet adhesion, *Ann. Biomed. Eng.* 49 (12) (2021) 3609–3620, <http://dx.doi.org/10.1007/s10439-021-02870-4>.
- [68] C.J. Spieker, G. Závodszy, C. Mouriaux, P.H. Mangin, A.G. Hoekstra, Initial platelet aggregation in the complex shear environment of a punctured vessel model, *Phys. Fluids* 35 (7) (2023) <http://dx.doi.org/10.1063/5.0157814>.
- [69] C.J. Spieker, K. Asteriou, G. Závodszy, Simulating initial steps of platelet aggregate formation in a cellular blood flow environment, in: *Computational Science – ICCS 2023*, Springer Nature Switzerland, 2023, pp. 323–336, http://dx.doi.org/10.1007/978-3-031-36024-4_26.
- [70] G. Závodszy, C. Spieker, B. Czaja, B. van Rooij, Cellular blood flow modeling with HemoCell, in: *Methods in Molecular Biology*, Springer US, 2023, pp. 351–368, http://dx.doi.org/10.1007/978-1-0716-3449-3_16.
- [71] A.L. Mescher, *Blood*, in: *Junqueira's Basic Histology: Text and Atlas*, 15e, McGraw-Hill Education, New York, NY, 2018, URL: accessmedicine.mhmedical.com/content.aspx?aid=1160662248.
- [72] P.A. Aarts, S.A. van den Broek, G.W. Prins, G.D. Kuiken, J.J. Sixma, R.M. Heethaar, Blood platelets are concentrated near the wall and red blood cells, in the center in flowing blood, *Arteriosclerosis* 8 (6) (1988) 819–824, <http://dx.doi.org/10.1161/01.ATV.8.6.819>, URL: <https://www.ahajournals.org/doi/10.1161/01.ATV.8.6.819>.
- [73] S.W. Schneider, S. Nuschele, A. Wixforth, C. Gorzelanny, A. Alexander-Katz, R.R. Netz, M.F. Schneider, Shear-induced unfolding triggers adhesion of von Willebrand factor fibers, *Proc. Natl. Acad. Sci.* 104 (19) (2007) 7899–7903, <http://dx.doi.org/10.1073/pnas.0608422104>, URL: <http://www.pnas.org/cgi/doi/10.1073/pnas.0608422104>.
- [74] H. Fu, Y. Jiang, D. Yang, F. Schefflinger, W.P. Wong, T.A. Springer, Flow-induced elongation of von Willebrand factor precedes tension-dependent activation, *Nature Commun.* 8 (1) (2017) 324, <http://dx.doi.org/10.1038/s41467-017-00230-2>, URL: <http://www.nature.com/articles/s41467-017-00230-2>.
- [75] C.E. Sing, A. Alexander-Katz, Elongational flow induces the unfolding of von willebrand factor at physiological flow rates, *Biophys. J.* 98 (9) (2010) L35–L37, <http://dx.doi.org/10.1016/j.bpj.2010.01.032>, URL: <https://linkinghub.elsevier.com/retrieve/pii/S0006349510001979>.
- [76] W. Bergmeier, R.O. Hynes, Extracellular matrix proteins in hemostasis and thrombosis, *Cold Spring Harb. Perspect. Biol.* 4 (2) (2011) a005132, <http://dx.doi.org/10.1101/cshperspect.a005132>.
- [77] S. Wessler, Thrombosis in the presence of vascular stasis, *Am. J. Med.* 33 (5) (1962) 648–666, [http://dx.doi.org/10.1016/0002-9343\(62\)90244-9](http://dx.doi.org/10.1016/0002-9343(62)90244-9).
- [78] E. Falk, Coronary thrombosis: Pathogenesis and clinical manifestations, *Am. J. Cardiol.* 68 (7) (1991) B28–B35, [http://dx.doi.org/10.1016/0002-9149\(91\)90382-u](http://dx.doi.org/10.1016/0002-9149(91)90382-u).
- [79] G. Giustino, A.J. Kirtane, P. Généreux, U. Baber, B. Witzenschnitzer, F.-J. Neumann, G. Weisz, A. Maehara, M.J. Rinaldi, C. Metzger, T.D. Henry, D.A. Cox, P.L. Duffy, E.L. Mazzaferri, B.R. Brodie, T.D. Stuckey, G.D. Dangas, D.P. Francese, C. Litherland, R. Mehran, G.W. Stone, Relation between platelet count and platelet reactivity to thrombotic and bleeding risk: From the assessment of dual antiplatelet therapy with drug-eluting stents study, *Am. J. Cardiol.* 117 (11) (2016) 1703–1713, <http://dx.doi.org/10.1016/j.amjcard.2016.03.001>.
- [80] T. Gori, A. Polimeni, C. Indolfi, L. Räber, T. Adriaenssens, T. Münzel, Predictors of stent thrombosis and their implications for clinical practice, *Nat. Rev. Cardiol.* 16 (4) (2018) 243–256, <http://dx.doi.org/10.1038/s41569-018-0118-5>.
- [81] B. Czaja, M. Gutierrez, G. Závodszy, D. de Kanter, A. Hoekstra, O. Eniola-Adefeso, The influence of red blood cell deformability on hematocrit profiles and platelet margination, *PLoS Comput. Biol.* 16 (3) (2020) e1007716, <http://dx.doi.org/10.1371/journal.pcbi.1007716>, URL: <https://dx.plos.org/10.1371/journal.pcbi.1007716>.